DOE/NASA/1028-78/19
NASA TM-78997

POWER TRAIN ANALYSIS FOR THE DOE/NASA 100-kW WIND TURBINE GENERATOR

Robert C. Seidel, Harold Gold,
and Leon M. Wenzel
National Aeronautics and Space Administration
Lewis Research Center

October 1978

Prepared for
U. S. DEPARTMENT OF ENERGY
Office of Energy Technology
Division of Distributed Solar Technology

DOE/NASA/1028-78/19
NASA TM-78997

POWER-TRAIN ANALYSIS FOR THE DOE/NASA 100-kW WIND TURBINE GENERATOR

Robert C. Seidel, Harold Gold,
and Leon M. Wenzel
National Aeronautics and Space Administration
Lewis Research Center
Cleveland, Ohio 44135

October 1978

Prepared for
U. S. DEPARTMENT OF ENERGY
Office of Energy Technology
Division of Distributed Solar Technology
Washington, D. C. 20545
Under Interagency Agreement E(49-26)-1028

SUMMARY

Progress in explaining variations of power experienced in the on-line operation of a 100-kW experimental wind turbine-generator is reported. Data are presented that show the oscillations tend to be characteristic of a wind-driven synchronous generator because of low torsional damping in the power train, resonances of its large structure, and excitation by unsteady and nonuniform wind flow. The report includes a dynamic analysis of the drive-train torsion, the generator, passive driveline damping, and active pitch control as well as correlation with experimental recordings. Experimental measurements of the system transfer function were made by disturbing the blade pitch angle. They compared well with the model dynamics up through the frequency of the first mode. Oscillations of power were experienced near the first-mode frequency and are explained as resulting from the first-mode resonance amplifying disturbances from, for example, blade asymmetries. Control of power about a set point used proportional-plus-integral feedback to the pitch actuator, and control gains were formulated for reducing disturbances up to frequencies less than the first mode. A fluid coupling installed in the high-speed shaft is one solution demonstrated for reducing the first-mode resonant amplification.

A predicted second-mode resonance at 3.5 hertz in the power train was not observed experimentally. A small effect of tower motion within the power train dynamics (an interaction not modelled) was observed experimentally. Experimentally observed variations in power at the two-per-rotor-revolution (2P) frequency were more than predicted. The larger 2P variation is suspected to be the impact of local turbulences not modelled. A wind feed-forward control scheme was employed, but failed to attenuate wind-speed-change effects as well as predicted because the anemometer measurement of wind speed used in the control was not well correlated with the wind speed at the rotor.

E-9413

INTRODUCTION

A 100-kW experimental wind turbine-generator, designated the Mod-0, is being used to identify and solve technical problems associated with large wind turbines. It is located near Sandusky, Ohio and has been operating since November, 1975 under the federal wind energy program directed by the Department of Energy. The National Aeronautics and Space Administration, Lewis Research Center, has provided design and test.

Significant variations of power output are present when the Mod-0 is synchronized to a utility network (on-line). Some variations occur because of random

wind speed fluctuations that are too high in frequency for automatic compensation through the blade pitch mechanism. Further, blade passage through nonuniform winds such as wind shear and tower blockage produces high frequency periodic input disturbances. Because the generator assumes a torsion spring-like quality when on-line, a spring-mass resonance in the power train can result. This resonance can be destructive of structure and power quality.

The oscillation of parallel connected synchronous generators is a persistent problem even in current utilities. As discussed in reference 1, problems range from power variations of a single generator relative to a utility grid to regional oscillations for interconnected networks across the United States. Approaches to oscillations from wind turbine synchronous generators are given in references 2 to 5. The possible implementation of a slip coupling is discussed in reference 2. A slip coupling adds damping to the power train but at the cost of more complexity and reduced efficiency. In reference 3, transients accompanying wind gusts, with a compliant and damped shaft between the turbine and the generator, are calculated. A compliant shaft smooths the higher frequency power variations and damping prevents resonant oscillations with no steady power loss. However, construction of a suitably soft and damped shaft is not easily achieved. The use of a comliant shaft to lower the first resonance to below the turbine rotation frequency is analyzed in reference 4; and a method for increased generator damping through a variable excitation control is described in reference 5.

This study examines the nature of the power variations and evaluates, through analysis and test, several passive drive-train coupling elements and active pitch controls. Only torsional power-train dynamics are considered, and the analysis utilizes a linearization of the nonlinear system about an operating point. The wind turbine generator is modelled as one machine on an infinite bus with constant generator field excitation. The report does not include discussion of induction generators, fly wheel inertias, and active damping through variable blade pitch and generator exciter controls.

SYSTEM DESCRIPTION

An overall view of the Mod-0 wind turbine is shown in figure 1. It is a two-bladed, horizontal axis machine with a rotor diameter of 38.1 meters (125 ft). The axis of the downwind rotor is mechanically yawed normal to the wind. The blades are aluminum NACA 23000 series airfoils with a twist of 34° from root to tip. The power train components, located inside the nacelle atop the tower, are shown in figure 2. The hub contains the hydraulic servo and bevel gears for collective pitch control. The low speed shaft supports the weight of the rotor through

bearings mounted to the bedplate and is connected to the gear box through a spring-type coupling (not shown). The gear box is a triple mesh of gears that increases the 40 rpm rotational speed of the low speed shaft by a factor of 45. The high-speed shaft transmits the torque through a parallel set of five V belts, nominally having a 1:1 speed ratio. The generator is a four pole, 125 kVA, 480 volt, synchronous generator rated for 100 kW at a 0.8 power factor.

Three high speed shaft configurations were analyzed in the test program: a stiff steel coupling, a softer spring elastomeric coupling, and a fluid slip coupling.

A block diagram of the power control feedback loop is shown in figure 3. A transducer measurement of the power is compared with set point power and the error signal sent to a proportional plus integral structured controller. The controller commands a pitch angle through the pitch actuator.

MODEL DESCRIPTION

The primary goal of the power train modelling was to describe the transfer function of generator power-to-blade disturbances for on-line operation.

Drive Train

A block diagram of the power train mechanical elements represented as lumped masses connected by torsion springs is shown in figure 4. The values of stiffness, inertia, internal damping, and external damping used in this model are listed in table I. The stiffness and inertia values are from a normal modes analysis of the Mod-0 wind turbine reported in reference 6. The aerodynamic damping of blade inplane motion, parameter D1, was estimated from curves of rotor power at different speeds and is relatively small, especially considering it represents the inherent damping available from the wind. The external damping values represent viscous losses from friction, windage, etc. which are based on a measured 80 percent power train efficiency. The relatively larger internal or material damping values are estimates based on an assumed 0.05 damping ratio in the higher modes.

Two sets of values are given for the elastomeric shaft. The parameters labeled "stiff" are the parameters for the physical elastomeric shaft tested. The set labeled "soft-damped" are for an assumed shaft with an overly optimistic damping. Its lower stiffness corresponds to the stiffness obtained from bench tests rather than the stiffness measured in actual wind turbine test operation. The shaft was instrumented to enable recording its windup while rotating at 1800 rpm. The higher stiffness recorded is believed to be the result of internal binding of the elastomeric shaft steel supports.

For the dynamics study, the blade model was a single mass and torsion spring. The spring stiffness was sized to give the 2.47 hertz frequency calculated for the blade first inplane mode from structural studies (ref. 7). A nominal value of one-half of the rigid body moment of inertia was assigned to the blade tip and the remainder to the hub. The sensitivity of this approximation is discussed later.

A block diagram of the generator electrical model connected to an infinite bus is shown in figure 5. The generator model is the voltage-behind-subtransient-reactance model, E", of reference 8.

Control

An active generator exciter control is not modelled. Field tests showed the exciter response to be slow; hence a constant voltage is used. An active variable blade pitch angle control is modelled. The pitch actuator is modelled as a double lag at 1.5 hertz based on test measurements of the actuator response.

The static performance predicted for the blades is given in figure 6. For a power-train efficiency of 80 percent, a 125-kW rotor power input produces a 100-kW electrical power output. The blade pitch gain, the slope of the power-pitch curve, is shown at two wind speeds. The blade pitch gain of 42 kW/deg at the higher wind speed is about four times greater than the gain at the lower wind speed. To be conservative, that blade gain of 42 kW/deg for the higher wind speed is used in controller gain designs. The disturbance gain for wind speed changes can also be inferred from figure 6. In the high winds it is 56 kW/m/s (26 kW/mph). In a wind feed forward control scheme to be discussed later, the correction in pitch used for a change in wind speed can be obtained from these gains as (56 kW/m/s)/(42 kW/deg) = 1.34 degrees of pitch change per meter per second change in wind speed.

Model Equations

A list of the report symbols, detailed mechanical and electrical model equations, and FORTRAN computer program listings are presented in appendixes A, B, and C, respectively.

The power-train model has two nonlinear elements: the stiffness of the low speed shaft coupling, and the electrical generator. However, a linear analysis was used throughout the study. The low speed shaft was linearized at the operating point power level, and the generator equations became linearized by numerically perturbing the state variables (in both directions) around an operating point.

The generator linearization was not particularly sensitive to the perturbation size for even a 20 percent change. System transfer functions and frequency responses were obtained using the programs of reference 9. In comparisons of experimental and analytical results, a few percent error may exist because the generator power and the generator torque were assumed proportional and were used interchangeably.

MODEL ANALYSIS

The analysis concerned primarily the transfer function of generator power-to-blade disturbances with different plant element dynamics and pitch control. Sensitivity studies were made for different blade tip inertias and generator electrical conditions.

Plant Dynamics - No Control

Frequency response magnitude plots of the transfer function of generator power-to-blade disturbances are shown in figure 7. Phase angle plots convey mostly redundant information and are not shown. Blade disturbances can result, for example, from angle of attack changes due either to changes in wind speed or pitch angle. Responses are shown for three high-speed shaft configurations: a stiff steel shaft, a soft-damped elastomeric shaft, and a slip coupling set to slip 2.3 percent at 100 kW. The responses are normalized to one at zero frequency and include no pitch control. The stiff steel shaft displays a large peak in the response at 0.69 hertz, a frequency very close to the one per rotor revolution (1P) frequency of 0.67 hertz. This resonance amplifies wind fluctuations and the periodic power variations due to, for example, any differences between blades. The peak is less with the slip and elastomeric couplings because of the damping the couplings provide.

From figure 7 it can be seen that the responses of the different configurations are about the same at the even multiples of rotor revolution frequency (2P, 4P, . . .). The largest difference occurs at the 2P frequency where the slip coupling response is about 50 percent lower than that of the stiff shaft. Thus it would be expected that the response to disturbances at frequencies above 2P would be nearly the same for all configurations.

The systems' first and second mode natural frequencies and damping ratios corresponding to the peaks in the magnitude response plot are listed in table II. It is seen that the different couplings affect primarily only the first mode damping ratio. The ratio increases from 0.097 for the stiff elastomeric coupling, to 0.10

for the stiff steel shaft, to 0.42 for the soft-damped elastomeric coupling, to 0.92 for the 2.3 percent slip coupling. Note that the damping ratio for the stiff elastomeric shaft is lower than for the stiff steel shaft, showing that a softer coupling lowers the resonant frequency but without enough damping may increase the resonant amplification.

As discussed, the blade tip moment of inertia was set to one-half of the blade's rigid body moment of inertia. System frequency responses with the slip coupling configuration for three blade tip inertias of 0.1, 0.5, and 1.0 of the rigid body inertia are plotted in figure 8. To keep the results comparable, the blade's natural frequency and damping ratio with the hub fixed and the total moment of inertia of the blade tip plus hub were held constant. It is seen that the second mode of the power train is sensitive to the tip mass. The smaller tip mass results in more peaking at a lower frequency.

In another sensitivity study, changes in the generator and electrical tie line conditions were investigated. The sensitivity analysis was for one machine on an infinite bus with no active exciter control. The conditions were changed one at a time from the power factor of 0.8 to 1.0, the power level of 100 kW to 10 kW, and from the external tie line reactance of 0.0103 per unit to 0.3 per unit. Results are considered for the stiff shaft configuration because of its initially low damping. The power train's first and second mode characteristics are listed in table III. The first mode damping ratio increases for increased power factor and decreases for decreased power. The sensitivity to all changes, however, is small.

Periodic Response

The periodic disturbances resulting from linear wind shear and tower blockage of the wind were calculated by the rotor aerodynamics program MOSTAB-WT (ref. 10). (In the MOSTAB program the blade is divided into 12 segments and allowed to move in the flap direction. The program assumes a rigid rotating hub with no blade torsional dynamics.) The time domain power variations calculated by MOSTAB for three different wind speeds are plotted in figure 9. In high winds the rotor power momentarily drops to less than half. The spectral components of the rotor power curves of figure 9 are plotted in figure 10. The curves have content only at the even multiples of rotor frequency (2P, 4P, . . .) which is the case for periodic disturbances to two symmetric blades.

A MOSTAB forcing function and the resulting responses in power output are shown in figure 11. The method used to obtain the power responses in the time domain was:

(1) Use MOSTAB to calculate the forcing function as a function of time.

(2) Take a Fourier transform of the forcing function.

(3) Multiply by the appropriate drive-train transfer function.

(4) Take an inverse Fourier transform of resulting product.

The responses obtained for the three high-speed shaft couplings appear similar. The output variation displays a 2P and a 4P component nearly equal in amplitude. The maximum excursion of power is about 7 kW from the mean.

The spectral magnitude components of the output power (from step 3 above) at the key (2P, 4P, . . .) periodic frequencies are plotted in figure 12 for the slip coupling configuration with no blade pitch control. These magnitudes are less than the MOSTAB disturbance given in figure 10 by the attenuation of the power train. Consistent with the time response description, the 4P components are as large as the 2P components.

Closed Loop Pitch Control

The proportional plus integral blade pitch controller was described in figure 3. System magnitude responses with closed loop pitch control are shown in figure 13 for the slip coupling configuration for a family of controller gains each having the proportional gain equal to one-half of the integral gain. For a given integral gain, that ratio nearly maximizes the damping ratio of the first mode. Depending on gain, the control attenuates disturbances to a value between 0.7 and 0.2 of their open loop value at a frequency of 0.1 hertz. At a frequency a decade lower the closed loop amplitude is about a decade lower because of the integral control action. All responses peak above the open loop amplitude before reaching the system first mode frequency. The peaking develops into a closed loop instability with sufficiently high gains at about 0.6 hertz. The effect of the control is not significant at the (2P, 4P, . . .) blade passing frequencies because the control bandwidth is less than the 2P frequency.

The effect of the controller with the stiff steel shaft is similar to results shown for the slip coupling if a filter set to notch out frequencies near the system first mode is used in the control. The notch filter used was a second order zero with a damping ratio of 0.1 (to cancel the system first mode) over a second order pole with a damping ratio of 1.0. Of course, the control does not remove the first mode resonance, which continues to exist, but the control does not excite this resonance. Without the notch filter the stiff high-speed shaft coupling is harder to control. For example, for system stability there can be no significant proportional gain and the integral gain must be low.

Wind Feed Forward Control

A wind feed forward control scheme using the wind speed signal as an open-loop input into the pitch angle control was investigaged as a means of attenuating the effect of wind speed changes. A schematic of the wind feed forward control is shown in figure 14. The anemometer used was insensitive to the wind direction and was located on the nacelle. It was about 4.6 meters upwind of the rotor and had about a 4.6-meter of air distance constant. These characteristics are modelled with an exponential lead and a lag. Figure 15, a cross plot of the data in figure 14, shows the pitch angle required to keep constant power for different wind speeds. The rated and low power curves shown have nearly the same slope, 1.342 deg/(m/s), thus one gain can approximate all power levels. The feed forward schedule is cut off for wind speeds below 8 m/s, and the output of the closed loop power control effectively biases the schedule up and down. A potential flaw in this scheme is that the wind speed measured by the relatively small anemometer may not be representative of the rotor average wind velocity.

The wind speed correction has dynamics because the signal must pass through the anemometer and pitch actuator dynamics. With an ideal measurement of the wind speed (one that is truly representative of the instantaneous blade average wind) and the assumed linear relation between wind speed and power, disturbances due to wind speed changes would be attenuated by the following factor

$$1 - \frac{e^{\frac{\text{distance upwind}}{\text{wind speed}} s}}{\left(\frac{\text{distance constant}}{\text{wind speed}} s + 1\right) (\text{actuator constant}\ s + 1)^2}$$

The frequency response magnitude of this expression is plotted in figure 16 for several wind speeds. It can be seen that the feed forward control theoretically should result in greatly reduced low frequency wind disturbance error and error reduction up to about 2 hertz.

RESULTS AND DISCUSSION

As part of the search for a better understanding of the Mod-0 power variations and the means to smooth them, experimental measurements of the power train dynamics were made and compared with model predictions. Measurements were made for the three high-speed shaft couplings, a range of controller gains, and with wind feed forward control. The transfer function of generator power output-to-rotor disturbance was the key relationship sought.

Transfer Function Measurement

To obtain data on the response of output power to rotor disturbances, the blade pitch angle was intentionally disturbed. In figure 17, a schematic block diagram of the setup used to disturb the blade pitch angle is shown. A signal from a random noise generator was summed into the pitch command. The resulting pitch disturbance provided data for transfer function measurements. About 25 minutes of data were recorded to achieve statistically good results for each test. The taped signals were either analog or sampled adequately to be nearly analog for frequencies of interest below 10 hertz. The reduction of data to its spectral content and transfer function relationships was performed using a spectrum analyzer (ref. 11).

For some tests in days of low winds, the generator was run as a motor driving the blades as a fan. Comparisons showed that whether the generator was run as a generator or as a motor did not significantly affect the transfer functions sought.

An example measurement of the transfer function of electric power output to pitch angle change is shown in figure 18. The data are most reliable near 0.5 and 2.0 hertz as indicated by the high coherence. That is, the output is attributable to the input and not to some other plant noise. Near zero frequency the coherence is low and the data are not reliable. The magnitude response does not hold a nearly constant value extending to zero frequency because wind speed changes compete with the test pitch disturbance. The action of the closed loop control is to suppress power changes. This occurred primarily at low frequencies where the wind's content is concentrated (ref. 12), and where the loop gain is highest because of the integral control. The coherence is also low near 0.7 and 1.3 hertz because of system 1P and 2P disturbances not related to the test disturbance. Beyond about 2.5 cps the coherence is generally near zero, and further results are reported to only 2.5 hertz.

There was no clear measurement of a system second mode resonance which the power train dynamic model would predict to be near 3.5 hertz. A second mode resonance would be indicated by a peak in the magnitude response accompanied by a phase shift of 180° and high coherence. In the sensitivity study, it was noted that the second mode peak decreased for increased inertia in the blade tip. However, it may not follow that the experimental nonobservance of a second mode can be used to increase the tip inertia because the cantilevered and tapered blade was represented by only a single mass.

Stiff steel shaft. - A transfer function measured in high winds with the stiff steel high-speed shaft (no slip coupling) and the corresponding model predictions are compared in figure 19. The vertical magnitude axis scale is linear to more clearly illustrate the large resonance. The resonant frequency, that frequency where the phase is -90° and the magnitude peaks, is seen to be 0.69 hertz which is also the calculated value. The experimental resonant peak is lower than that predicted by the model. The experimental first mode damping ratio is estimated to be 0.22 which is more damping than the calculated value of 0.10 (table II). Increased damping could result from slippage in the V belts. About 0.3 percent slip was found; but it was not very repeatable. A 0.3 percent viscous slip in the model results in a 0.2 damping ratio but lowers the calculated first mode frequency lower than the measured value. Alternative explanations include presuming the generator has more damping than calculated. It is more likely, however, that nonlinearities become important for large swings in power. Nonlinearities in a system may appear to decrease a resonance because power input at one frequency may shift upon output to different frequencies and thus be missed in the data reduction.

Stiff elastomeric shaft. - A measured and calculated transfer function with the stiff elastomeric high-speed shaft is shown in figure 20. A large first mode resonant peak, similar to the results with the steel shaft, is evident in the plot. The observed resonant frequency is 0.54 hertz which is also the calculated frequency. From the transfer function magnitude and phase characteristics, the first mode damping ratio is estimated to be 0.22, which is more damped than the calculated value of about 0.1. It is noted that experimentally, both the elastomeric and the steel shaft responses give a damping ratio of about 0.22. Slip in the V belts in the motoring mode where the elastomeric shaft test was run was much less than the 0.3 percent slip quoted for the steel shaft. The likely explanation for the greater apparent damping again being that, for large swings in power, nonlinearities in the system appear to reduce the resonant peak.

Slip coupling. - The calculated and measured system transfer functions for the slip coupling set to slip 1.5 and 4.7 percent at 100 kW are compared in figures 21 and 22, respectively. The predicted responses are in good agreement through the first mode resonance of about 0.5 hertz. Near 2 hertz there exists a difference of about 10 dB or a factor of 3. This is discussed next.

Tower interaction. - In previous transfer function magnitude comparisons the amplitude responses of the model were lower than the experimental data near 2 hertz. Because measurements of tower motion correlate well with power variations near that frequency it is believed that there is tower interation. Three accelerometers were mounted in perpendicular planes on the rear main bearing

support of the low speed shaft. Only the horizontal yaw results are reported; the other two planes were similar. To show the effect of tower motion on the power train, the path is broken into two parts. First, the response of tower acceleration-to-pitch is shown in figure 23, and then the response of power-to-tower acceleration is shown in figure 24. Judging from the coherences, this path is important only near 2 hertz where tower natural frequencies are excited. At 1.85 hertz it is interesting to note that "acceleration-to-pitch" (0.18 g/deg) times "power-to-acceleration" (107 kW/g) equals 19 kW/deg. This 19 kW/deg compares well with the direct value obtained from figure 21 of about 17 kW/deg measured (and 6 kW/deg calculated). Thus, with good coherence, the tower motion path accounts for the higher response magnitude. Fortunately, tower motion does not cause a serious problem for the Mod-0 because it occurs at a relatively high and well placed frequency in comparison with the major excitation forces.

Control gains. - The effect of the controller on the closed loop response of power-to-pitch command is shown in figures 25 and 26. Figure 25 was run at normal values of proportional and integral gain while in figure 26 the gains were increased by a factor of 6. Calculated responses are shown in both cases; it is noted that the analytical and experimental results agree well. The response with the high gain controller exhibits better low frequency attenuation but it is more resonant. The actual system was nearly unstable; it oscillated out of synchronism moments after completing the test tape. The model with that high gain was unstable. The phase response calculations are shown to only the frequency of instability. Obviously the control gain needs to be some compromise between attenuation at low frequency and amplification near the first mode.

Wind feed forward. - Operational data recordings of the slip coupling configuration were made with and without wind feed forward control. Comparisons varied because of wind differences between runs and it was difficult to isolate the effect of the feed forward control. A comparison of the coherences of the responses of "power-to-the measured wind speed" is shown in figure 27. The argument for wind feed forward is that it should decrease any relation between wind and power. It is seen that in both cases the coherence is mostly low and the transfer function data are not reliable. The coherence with feed forward showed a lower relation at the very low frequencies but a generally higher relation up to 1 hertz. This would indicate that the feed forward as implemented was increasing rather than decreasing power excursions resulting from unsteady wind conditions over a broad frequency range. This is attributed to the single, relatively small wind speed sensor not being a reliable indication of the instantaneous average wind over the circle of area swept out by the blades.

Power Time History

Sample time history traces of Mod-0 power variations about a 100-kW set point are shown in figures 28(a) and (b). The power dropped below the set point sometimes because there was not enough wind. In circled areas labeled "over power", the power peaked to near 150 kW. In the figure 28(a), the case without wind feed forward, the overshoot was apparently in response to a gust of wind. It is noted that control action subsequently reduced the power level although the wind speed remained high. In figure 28(b), the case with wind feed forward, the power overshoot occurred in response to a drop in the measured wind speed! Apparently, the feed forward control over-corrected because the measured drop in local wind was not representative of the blade average wind speed. Unlike the model calculations of figure 11, the power exhibits oscillations at a frequency of 2P fading in and out The 2P oscillations have at times about a 20-kW zero-to-peak amplitude for both low and high winds. This 20-kW (maximum) amplitude compares poorly to a predicted (mean) amplitude of only 1.2 kW in a 8.9 m/s wind from figure 12.

Spectral Analysis of Power

A frequency domain spectral analysis of generator power measurements is shown in figure 29. The peak at the odd 1P multiple exists because, as was found, the blades were not pitched the same by a difference of 1.7^{o}. The source of the peaks labeled "X" at 2.56 hertz and at twice that frequency has not as yet been identified. There are peaks at the even multiples of the blade passing frequencies (2P, 4P, . .). The 2P peak differs qualitatively from the others in that it is much broader. This may suggest that nonlinear or higher order couplings exist. Another possibility is that the flow field has random local distortions over only part of the blade area and lasting only a few revolutions so as to modulate the periodic power around the 2P frequency. The buildup around the 2P peak was observed "real-time" during the data reduction. It appeared to be random, lending support to assumed unsteady local wind turbulence.

In figure 30, the frequency content in the peaks of the spectrum of figure 29 are compared with model predictions. The experimental peaks are not a single frequency as in the analytical case. The effective content of the broad peaks was calculated as the square root of the sum of the squares of individual analyzer readings. The analytical points were values from figure 12 divided by the square root of two to convert zero-to-peak sinusoidal amplitude to root mean square power. The comparison shows good agreement at the 4P and 6P frequencies, but there is much more content in the experimental data at 2P and 8P. The 8P content

was small enough and at a high enough frequency to be insignificant. The average 2P output power content, about 4 kW rms, is about four times that predicted and is discussed further.

Power oscillation at the 2P frequency has just been shown higher than that predicted using input from MOSTAB for a fixed hub applied as a schedule to the power train torsional model. An insight is that the 2P power correlates well with the blade flatwise bending moment (a nontorsional moment and not in the model). Transfer function data between power and blade flatwise bending moment, from experimental data recorded during normal operation are shown in figure 31. Because the coherence is high near the 2P frequency, it can be concluded that the 2P power variations result probably from a forcing function and not some unknown torsional resonance. A 2P forcing function not considered in the MOSTAB calculations is nonlinear wind shear. The MOSTAB calculations assumed a linear wind shear of plus and minus 15 percent of the hub wind speed. This linear shear causes little net aero-torque variations as blade differences cancel. However, a quadratic shear with power portional to wind speed would increase the aero-torque variations. A calculation that does not include inertial effects from flap dynamics shows quadratic shear could about double the 2P spectrum content (add a 7.5 kW sinusoid to the 2P rotor input or 1.3 kW rms to the 2P generator output). Another possible source of 2P power variation not considered in the MOSTAB calculations are random local turbulences.

CONCLUDING REMARKS

1. Oscillation of electric power near the one-per-rotor-revolution frequency (1P) was evident during early on-line tests of the Mod-0 with the stiff high-speed shaft. This was found to result from a torsional power-train resonance near the 1P frequency having only a 0.10 damping ratio. The resonance-amplified 1P noise resulting from nonsymmetric blade-pitch settings. The control system (when without a first-mode notch filter implemented) further increased the oscillation. The frequency of the first mode depends upon the power-train torsional spring rate. To shift the resonant frequency away from the 1P frequency and to add damping to the system so as to reduce the amplification, different high-speed shaft couplings were studied. The calculated damping ratio of the first mode increased to 0.42 for a soft-damped elastomeric coupling and to 0.92 for a fluid coupling set to slip 2.3 percent at 100 kW. Experimental measurements of the system transfer function compared well with linear-model dynamics up through the frequency of the first mode. In particular, the ability of the slip coupling to damp the first mode in comparison with the stiff shaft was demonstrated experimentally.

2. Although the model predicted a significant resonance from the second mode of the power train, there was no clear measurement proving its existence.

3. A small tower motion was observed experimentally. However, tower motion was not part of the power-train model.

4. The measured power content near the two-per-revolution (2P) frequency was broadband and had some four-times-greater content than predicted. The larger 2P power may result from local turbulences acting over only part of the blade area.

5. In a sensitivity analysis, dynamics of the power-train model (with constant generator excitation) were not significantly affected by small variations of the generator and electrical parameters of power level, power factor, and tie-line reactance.

6. Closed-loop pitch controller proportional-plus-integral-feedback gains were formulated that could attenuate low-frequency disturbances but only up to frequencies less than the system first mode. Excessively high gains drove the system toward instability at about 0.6 hertz.

7. Analysis of a wind feed-forward control scheme using a wind-speed signal to command pitch indicated virtual elimination of low-frequency wind effects and attenuation to frequencies well beyond the system first mode. But the large advantage predicted was not seen, on the average, experimentally because the measured wind speed did not represent the instantaneous wind speed past the rotor blades.

APPENDIX A

SYMBOLS

C	torque conversion, N-m/P.U.
D	external damping, N-m/(rad/sec)
d	direct axis
d	internal damping, N-m/(rad/sec)
E	rms EMF, P.U.
E_{FD}	field EMF, P.U.
F	torque, N-m
I	rms current, P.U.
J	inertia, N-m/sec^2
j	imaginary number
K_1, K_2, K_d	constants
k	spring rate, N-m/rad
P	rotor frequency
q	quadrature axis
R	resistance, P.U.
R_g	gear ratio
r	reference axis
r_a	armature resistance, P.U.
s	Laplace variable, sec^{-1}
T	time constant, sec
T_b	blade torque, N-m
T_e	electrical torque, N-m
V	voltage, P.U.
v	wind velocity, m/s
X	reactance, P.U.
X_{xd}	constant

x synchronous reactance, P.U.

x_{ad} mutual armature damper circuit reactance, P.U.

Y admittance, P.U

β angle between V_∞ and V_a, rad

β pitch angle, deg

δ angle between quadrature and reference axis, rad

δ'' angle between E'' and reference axis, rad

θ angle between reference axis and I_a, rad

λ_D stator rms subtransient flux linkage, P.U.

φ angle between I_a and V_a, rad

Subscripts:

a armature

d direct axis

e external

IC initial condition

q quadrature axis

r reference axis

t terminal

x conjugate direction to r axis

0 open circuit

1 first blade

2 second blade

3 hub and low speed shaft

4 gear box and high-speed shaft

5 first pulley and "V" belts

6 second pulley and generator

∞ infinite bus

Superscripts:

' transient

'' subtransient

^ summed impedance

APPENDIX B

MODEL

Mechanical Model

The differential equations of the mechanical model of the Mod-0 power train shown in figure 5 are listed below for a perturbation about an operating point.

$$J_1\ddot{\theta}_1 = F_1 - D_1\ddot{\theta}_1 + T_b$$

$$J_1\ddot{\theta}_2 = F_2 - D_1\dot{\theta}_2$$

$$J_3\ddot{\theta}_3 = F_3 - F_1 - F_2 - D_3\dot{\theta}_3$$

$$J_4\ddot{\theta}_4 = R_gF_4 - F_3 - R_gD_4\dot{\theta}_4$$

$$J_5\ddot{\theta}_5 = F_5 - F_4 - D_5\dot{\theta}_5$$

$$J_6\ddot{\theta}_6 = -F_5 - D_6\theta_6 - \left[\left(T_e - T_e\right)_{IC}\right]C$$

where the forces F_i between the inertias are

$$F_1 = k_1(\theta_3 - \theta_1) + d_1\left(\dot{\theta}_3 - \dot{\theta}_1\right)$$

$$F_2 = k_1(\theta_3 - \theta_2) + d_1\left(\dot{\theta}_3 - \dot{\theta}_2\right)$$

$$F_3 = k_3(\theta_4 - \theta_3) + d_3\left(\dot{\theta}_4 - \dot{\theta}_3\right)$$

$$F_4 = k_4(\theta_5 - R_g\theta_4) + d_4\left(\dot{\theta}_5 - R_g\dot{\theta}_4\right)$$

$$F_5 = k_5(\theta_6 - \theta_5) + d_5\left(\dot{\theta}_6 - \dot{\theta}_5\right)$$

Generator Model

The differential equations for the generator model shown in the figure 7 block diagram are listed next.

$$T_e = E''_d I_d + E''_q I_q$$

$$T''_{q0}\dot{E}''_d = -E''_d - (x_q - x'')I_q$$

$$T''_{d0}\dot{\lambda}_D = -\lambda_D + E'_q + (x'_d - x_\ell)I_d$$

$$T'_{d0}\dot{E}'_q = -E'_q(1 + K_d) + X_{xd}I_d + K_d\lambda_D + E_{FD}$$

$$E''_q = K_1 E'_q + K_2\lambda_D$$

$$I_d = Y\left[-\hat{R}(V_{\infty d} - E''_d) + \hat{X}''(V_{\infty q} - E''_q)\right]$$

$$I_q = -Y\left[\hat{X}''(V_{\infty d} - E''_d) + \hat{R}(V_{\infty q} - E''_q)\right]$$

where

$$\hat{R} = r_a + R_e$$

$$\hat{X}'' = x'' + X_e$$

$$V_{\infty d} = -V_\infty \sin(2\theta_6 + \delta_{IC})$$

$$V_{\infty q} = V_\infty \cos(2\theta_6 + \delta_{IC})$$

$$Y = 1\Big/\left[(\hat{R})^2 + (\hat{X}'')^2\right]$$

$$K_1 = (x'' - x_\ell)/(x'_d - x_\ell)$$

$$K_2 = 1 - K_1$$

$$K_d = (x_d - x'_d)(x'_d - x'')\Big/(x'_d - x_\ell)^2$$

$$X_{xd} = (x_d - x'_d)(x'' - x_\ell)/(x'_d - x_\ell)$$

Model electrical parameters are given in table IV. The external tie line resistance and reactance values listed are for the Mod-0 Plum Brook Station location. The following four parameters listed were estimated as follows.

$$x'' = (x''_d + x''_q)/2$$

$$T''_{d0} = T''_d(x'_d/x''_d)$$

$$T'_{d0} = T'_d(x_d/x'_d)$$

$$x_\ell = x_d - x_{ad}$$

INITIAL CONDITIONS

The assumed known initial variables were not model states but the machine power, the power factor $\cos \varphi$, and voltage of the infinite bus V_∞. An initial condition phase diagram is given in figure 32. The model values derived are in the direct-quadrature axis which is a rotated mirror image of the reference bus axis.

An estimate of current I_a is

$$I_a \cong \text{machine power}/(V_\infty \cos \varphi)$$

The power into the infinite bus is the machine power minus the transmission line ohmic loss.

$$\text{bus power} = \text{machine power} - R_e I_a^2$$

The current I_r in phase with this power is

$$I_r = \text{bus power}/V_\infty$$

The derivation of the I_x component follows. The coordinates of V_a from figure 32 (or p. 161 of ref. 8) using complex arithmetic are

$$V_a = V_\infty + I_a(R_e + jX_e)$$

$$V_a = V_\infty + (I_r + jI_x)(R_e + jX_e)$$

$$V_a = (V_\infty + I_r R_e - I_x X_e) + j(I_x R_e + I_r X_e)$$

The angle β between V_a and V_∞ is

$$\beta = \tan^{-1}(\text{Imag } V_a/\text{Real } V_a)$$

$$\beta = \tan^{-1} \frac{I_x R_e + I_r X_e}{V_\infty + I_r R_e - I_x X_e}$$

The power factor angle φ between I_a and V_a is the arc cosine of the power factor.

$$\varphi = \cos^{-1} (\text{power factor})$$

From figure 32

$$\varphi = \beta - \theta$$

where θ is the angle of I_a with the reference or

$$\theta = \tan^{-1}(I_x/I_r)$$

Thus

$$\tan \varphi = \tan(\beta - \theta) = \frac{\tan \beta - \tan \theta}{1 + \tan \beta \tan \theta}$$

which after substitution for θ and β can be solved for I_x.

$$I_x = -V_\infty \pm \sqrt{\frac{V_\infty^2 - 4(-X_e + R_e \tan \varphi)\left(-I_r^2 X_e + I_r\right)(V_\infty + R_e I_r)\tan \varphi}{2(-X_e + R_e \tan \varphi)}}$$

The sign of the quadratic used was that for the minimum I_x (a negative number).

From figure 32 the F'' and E_{qa} vectors with respect to the reference axis are

$$V_a = V_\infty + I_a(R_e + jX_e)$$

$$E'' = V_a + I_a(r_a + jx'')$$

$$E_{qa} = V_a + I_a(r_a + jx_q)$$

These variables are related to the model d-q axis. The electrical angle δ between the q and r axes is

$$\delta = \tan^{-1}(\text{Imag } E_{qa}/\text{Real } E_{qa})$$

The angle δ'' of the E'' vector to reference is

$$\delta'' = \tan^{-1}(\text{Imag } E''/\text{Real } E'')$$

From figure 32 geometry

$$E''_q = |E''| \cos(\delta - \delta'')$$

$$E''_d = -|E''| \sin(\delta - \delta'')$$

$$I_d = -|I_a| \sin(\delta - \theta)$$

$$I_q = |I_a| \cos(\delta - \theta)$$

The other initial conditions can be found by setting the state equations to zero. The λ_D state equation and the E''_q equation are two equations in two unknowns.

$$-\lambda_D + E'_q + (x'_d - x_\ell)I_d = 0$$

$$K_1 E'_q + K_2 \lambda_D - E''_q = 0$$

with solutions

$$E'_q = E''_q - K_2(x'_d - x_\ell)I_d$$

or using the definition of K_2

$$E'_q = E''_q - (x'_d - x'')I_d$$

and

$$\lambda_D = E'_q + (x'_d - x_\ell)I_d$$

The E'_q state equation solved for E_{FD} is

$$E_{FD} = E'_q(1 + K_d) - X_{xd}I_d - K_d\lambda_D$$

The set of numerical values for the figure 32 nominal operating point and parameters of table IV are listed below.

Machine power, P.U.	≈0.8
Power factor	0.8
V_∞, P.U.	1
$I_a(r,x)$	(0.7953, -0.5898)
$V_a(r,x)$	(1.0098, -0.0054)
$E_{qa}(r,x)$	(1.6517, 0.8411)
$E''(r,x)$	(1.1188, 0.1225)
δ, rad	0.4710
δ'', rad	0.1090
T_e, P.U.	0.8176
I_r, P.U.	0.7953
I_x, P.U.	-0.5898
E''_d, P.U.	-0.3985
E''_q, P.U.	1.0525
[illegible]ad	0.6381
I_d, P.U.	-0.8865
I_q, P.U.	0.4411
E'_q, P.U.	1.0565
λ_D, P.U.	0.9546
E_{FD}, P.U.	2.8694

APPENDIX C

COMPUTER SUBROUTINES

Computer subroutines written in FORTRAN generated the initial conditions and state derivatives for a linear analysis package. These subroutines are listed in figures 33 and 34.

The FORTRAN symbols which are unlike the report symbols are defined below.

$Z(1) = \theta_1$	$Z(11) = \theta_6$
$Z(2) = \dot{\theta}_1$	$Z(12) = \dot{\theta}_6$
$Z(3) = \theta_2$	$Z(13) = E''_d$
$Z(4) = \dot{\theta}_2$	$Z(14) = \lambda_D$
$Z(5) = \theta_3$	$Z(15) = E'_q$
$Z(6) = \dot{\theta}_3$	$Z(16) = T_e$ (lagged at 10 Hz)
$Z(7) = \theta_4$	$Z(17) = \beta$
$Z(8) = \dot{\theta}_4$	$Z(18) = \dot{\beta}$
$Z(9) = \theta_5$	Z(19) = controller state
$Z(10) = \dot{\theta}_5$	

$CD1 = D_1$, etc.	$K11 = k_1$
$D1 = d_1$, etc.	$R1 = R_g$
$DLT = \delta''$	$TM = T_{e_{IC}}$

The F vector is the derivative of the Z vector. For example, $F(1) = \dot{\theta}_1$ and $F(2) = \ddot{\theta}_1$. Other constants are

B = 2/0.112 servo damping

CONVRT (in-lb/P.U.) = torque high speed shaft

Gain (in-lb/P.U.) = transducer gain $\frac{10}{150}$ V/kW $\times$ servo gain (9.4 deg/V)

$\times$ blade gain (42.5 kW/deg) $\times$ convert (5869 in-lb/P.U.)

$\times$ speed ratio R_g (45 rpm/rpm

REFERENCES

1. Symposium on Adequacy and Philosophy of Modeling: Dynamic System Performance. 1975 Winter Meeting. IEEE, N. Y., 1976.

2. Wind Turbine Project. New York Univ., Engineering Research College, for Office of Production Research and Development, War Production Board, W.P.B.-144, Washington, D.C., Jan. 31, 1946.

3. Johnson, Craig C.; and Smith, R. T.: Dynamics of Wind Generators on Electric Utility Networks. IEEE Trans. Aerosp. Electron. Syst. Vol. AES-12, no. 4 July 1976, pp. 483-493.

4. Mirandy, L. P.: Rotor/Generator Isolation for Wind Turbines. AIAA Paper 77-372. Mar. 1977.

5. Barton, Robert S.: Mod-1 Wind Turbine Generator Analysis. Wind Turbine Structural Dynamics. NASA CP-2034, 1977, pp. 167-178.

6. Sullivan, T. L.; Miller, D. R.; and Spera, D. A.: Drive Train Normal Modes Analysis for the ERDA/NASA 100-Kilowatt Wind Turbine Generator. NASA TM-73718, 1977.

7. Chamis, C. C.; and Sullivan, T. L.: Free Vibrations of the ERDA-NASA 100 kW Wind Turbine. NASA TM X-71879, 1976.

8. Anderson, P. M.; and Fouad, A. A: Power System Control and Stability. Vol. 1. The Iowa State University Press, 1977.

9. Seidel, Robert C.: Computer Programs for Calculation of Matrix Stability and Frequency Response from a State-Space System Description. NASA TM X-71581, 1974.

10. Hoffman, John A.; and Holchin, Barry W.: Modifications to MOSTAB for Wind Turbine Applications. MRI-2711, Mechanical Research, Inc., 1974.

11. Instruction Manual for the Model O-FFT 400, OMNIFEROUS Fast Fourier Transform Analyzer System. Nicolet Scientific Corporation, Northvale, N.J., 1976.

12. Lumley, J. L.; and Panofsky, H. A.: The Structure of Atmospheric Turbulence. Interscience Publishers, 1964.

TABLE I. - MECHANICAL PARAMETERS

(a) SI units

Station subscript	Inertia J, N-m-sec^2	Stiffness k, N-m/rad	Internal damping d, $\frac{\text{N-m}}{\text{(rad/sec)}}$	External damping D, $\frac{\text{N-m}}{\text{(rad/sec)}}$
1	31 930	7 682 968	33 895	3051
3	64 686	[a]558 477$\sqrt{\text{kW}}$	2 260	114
Four 2.3 percent slip	2 859	0	131	.113
Four steel	1 154	75 474	21	.113
Four elastomeric (soft-damped)	1 154	654	366	.113
Four elastomeric (stiff)	1 154	3 054	122	.113
Five slip	1.69	20 337	17	.07
Five no slip	.86	20 337	17	.07
6	.11	------	---	.18

(b) U.S. customary units

Station subscript	Inertia J, lbf-in-sec^2	Stiffness k, lbf-in/rad	Internal damping d, $\frac{\text{lbf-in}}{\text{(rad/sec)}}$	External damping D, $\frac{\text{lbf-in}}{\text{(rad/sec)}}$
1	282 600	68 000 000	300 000	27 000
3	572 520	[a]4 943 000$\sqrt{\text{kW}}$	20 000	1 010
Four 2.3 percent slip	25 300	0	1 160	1.0
Four steel	10 210	668 000	186	1 0
Four elastomeric (soft-damped)	10 210	5 790	3 240	1.0
Four elastomeric (stiff)	10 210	27 039	1 080	2.0
Five slip	15	180 000	150	.62
Five no slip	7.6	180 000	150	.62
6	24.2	------	---	1 6

[a]Linearized about steady state. Curve fit to stiffnesses of low speed shaft plus Falk coupling plus gears.

TABLE II. - SYSTEM RESONANCES - NO CONTROL

Configuration	First mode		Second mode	
	Natural frequency, cps	Damping ratio	Natural frequency, cps	Damping ratio
2.3 Percent slip at 100 kW	0.430	0 920	3.495	0.063
Elastomeric (soft-damped)	.516	.420	3.533	.058
Elastomeric (stiff)	.582	097	3.522	.056
Stiff steel	.689	.104	3.540	.056

TABLE III. - POWER TRAIN (STIFF SHAFT) SENSITIVITY TO ELECTRICAL FACTORS

Variable	First mode		Second mode	
	Natural frequency, cps	Damping ratio	Natural frequency, cps	Damping ratio
Nominal[a]	0.689	0.104	3.54	0.0558
Power factor = 1	.713	.192	3.55	.0551
$X_e = 0.3$	.641	.080	3.50	.0537
Power = 11 kW (no change in k_3)	.570	.067	3.49	.0684

[a]Nominal conditions are power factor = 0.8, external reactance, $X_e = 0.0103$, power = 103 kW.

TABLE IV. - ELECTRICAL PARAMETERS

T''_d, sec	0.0085
T''_{q0}, sec	0.062
T'_d, sec	0.145
T''_{d0}, sec	0.011
T'_{d0}, sec	1.942
x''_d, P.U.	0.128
x'_d, P.U.	0.165
x_d, P.U.	2.21
x''_q, P.U.	0.193
x_ℓ, P.U.	0.05
x_{ad}, P.U.	2.16
x'', P.U.	0.1605
K_1, P.U.	0.961
K_2, P.U.	0.039
K_d, P.U.	0.696
X_{xd}, P.U.	1.965
r_a, P.U.	0.018
R_e, P.U.	0.00466
X_e, P.U.	0.01031
V_∞, P.U.	1
Base kilovolt-amperes, kVA	125
Base voltage, V	480
Base ohms, ohms per phase wye	1.843

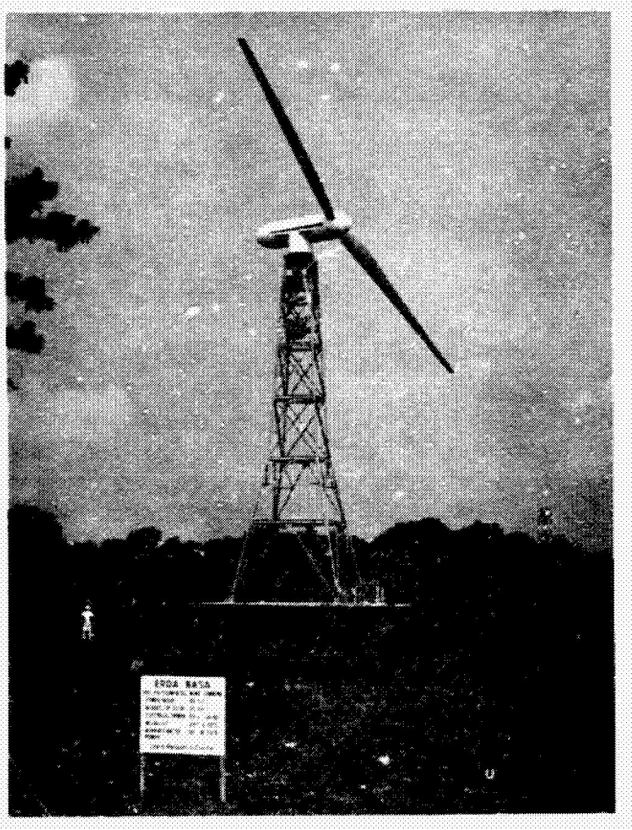

Figure 1. - Mod-0 100-kW wind turbine generator.

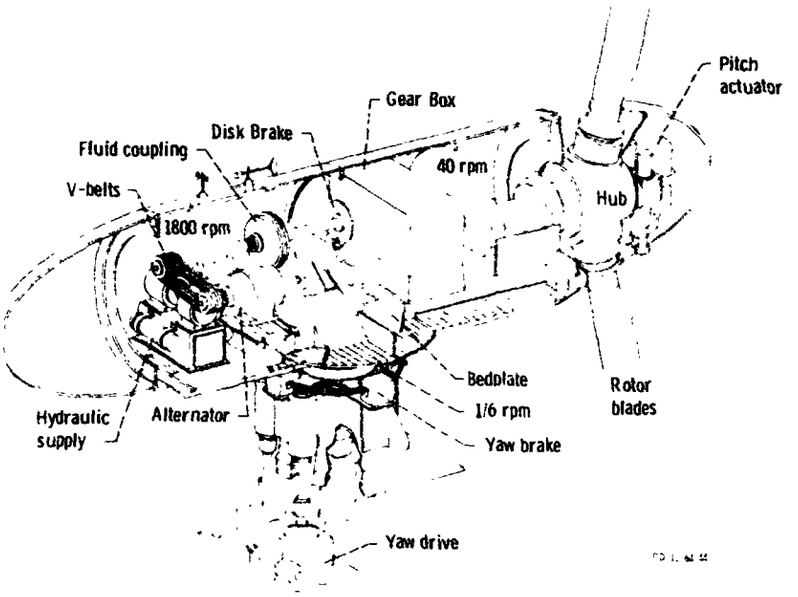

Figure 2 - Mod-0 turbine generator schematic of nacelle interior.

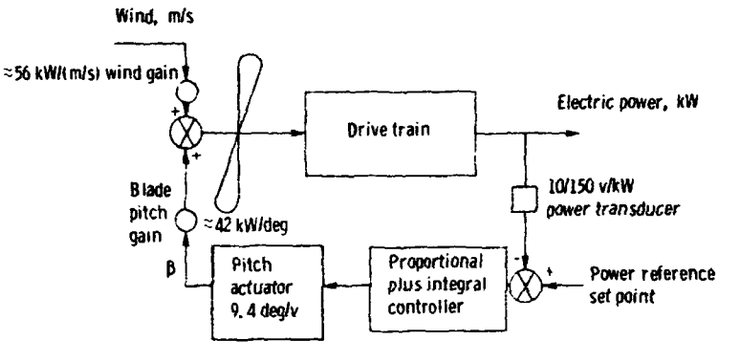

Figure 3. - Block diagram of closed loop power control.

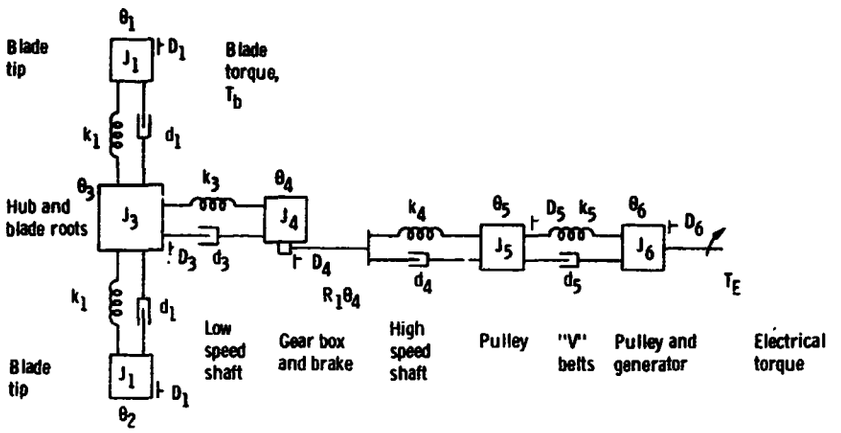

Figure 4. - Block diagram of simplified power train model showing inertial masses and torsional springs and dampers.

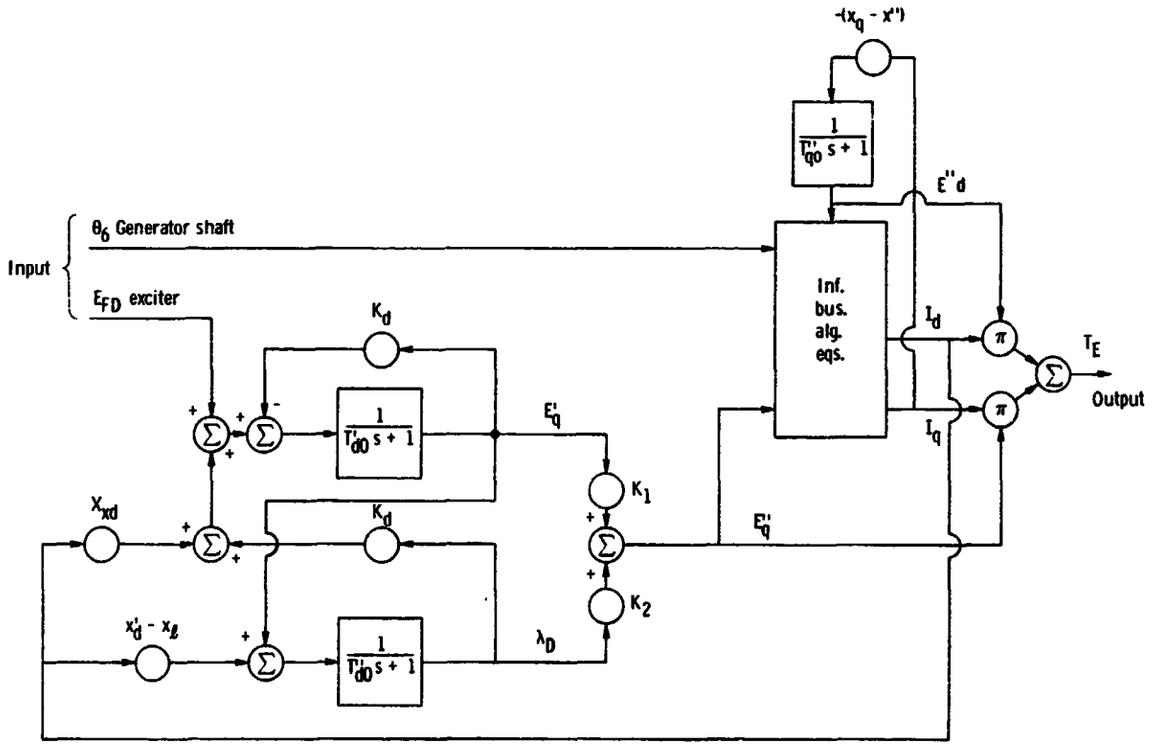

Figure 5. - Block diagram of generator third order dynamic model connected to an infinite bus through algebra equations.

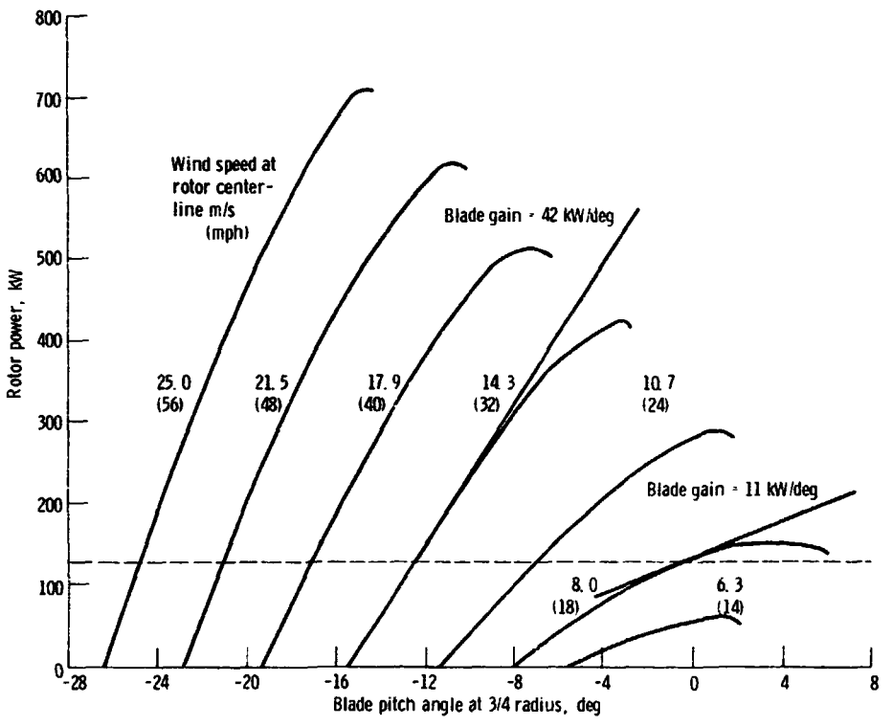

Figure 6. - Rotor performance map. Operating point tangents show blade gain at two wind speeds.

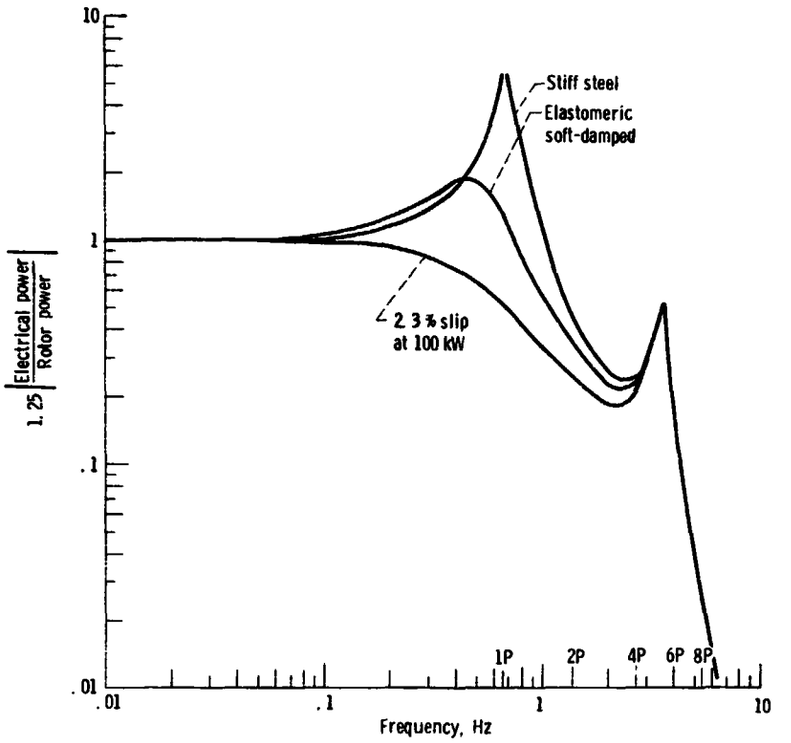

Figure 7. - Power train frequency response magnitude comparisons for three high speed shaft configurations

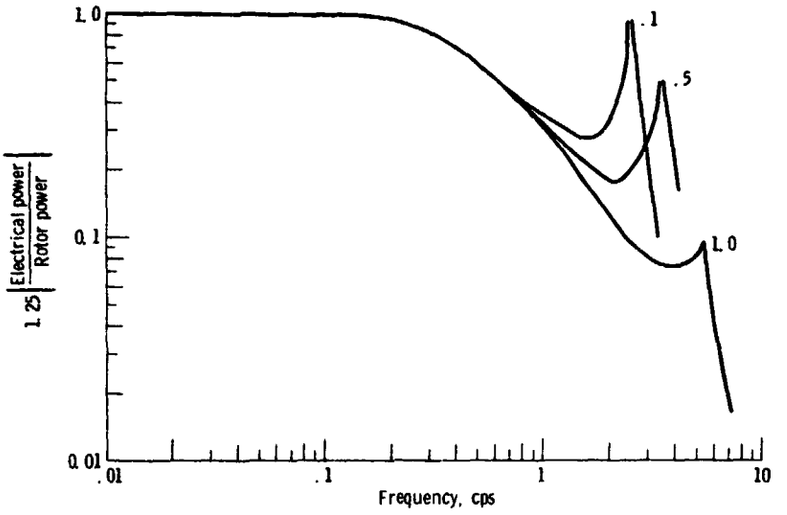

Figure 8. - Sensitivity study showing second mode variation in system frequency response magnitude comparisons for three blade tip masses given as fraction of blade rigid body moment of inertia. Slip coupling in high speed shaft slip rate of 2.3 percent at 100 kW.

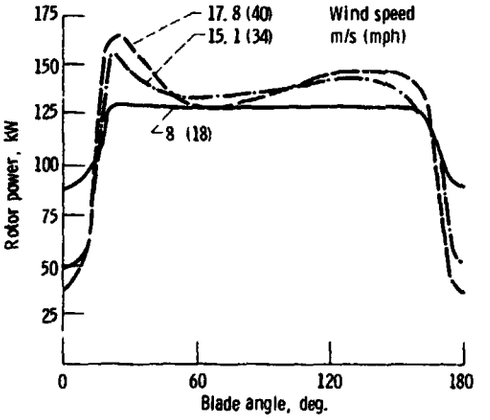

Figure 9. - MOSTAB rotor power versus blade azimuth for one-half revolution. Tower blockage assumed to reduce free stream velocity 28 percent over 30-degree arc. Blades vertical at 0^{0} and 180^{0}.

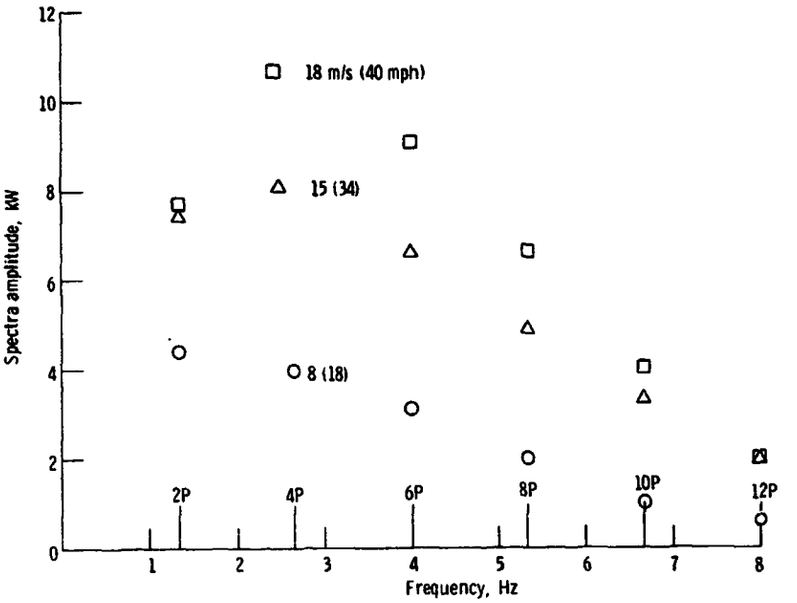

Figure 10. - MOSTAB rotor power zero-to-peak sinusoidal spectral components for three wind speeds.

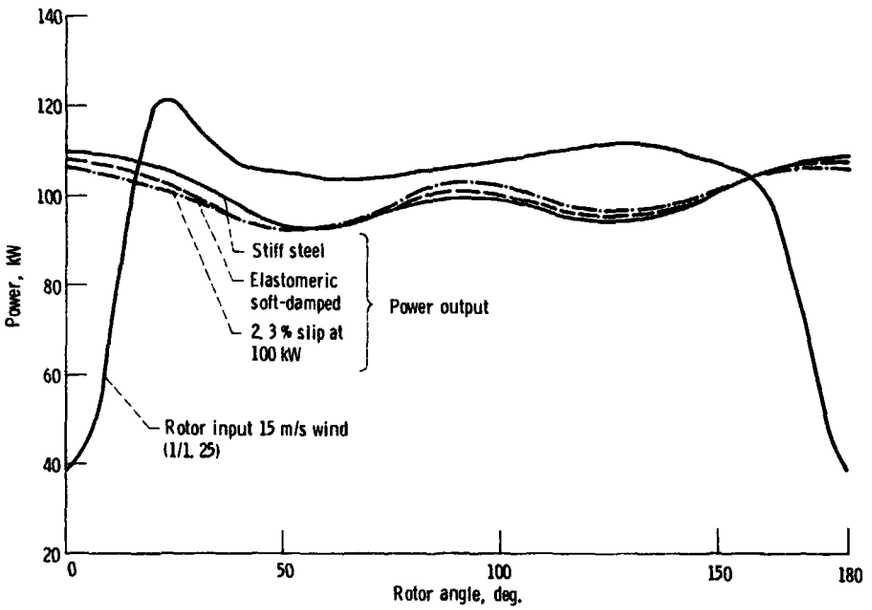

Figure 11. - Time response comparisons of power output with three high speed shaft configurations to MOSTAB rotor power input.

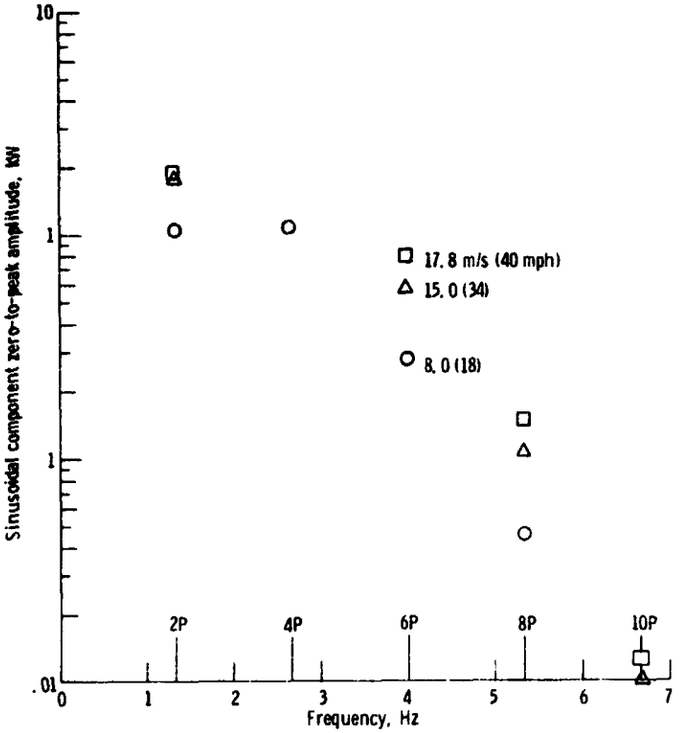

Figure 12. - Calculated spectral content of power output (with 2.3 percent slip at 100 kW in slip coupling) in response to MOSTAB rotor power input for three wind speeds.

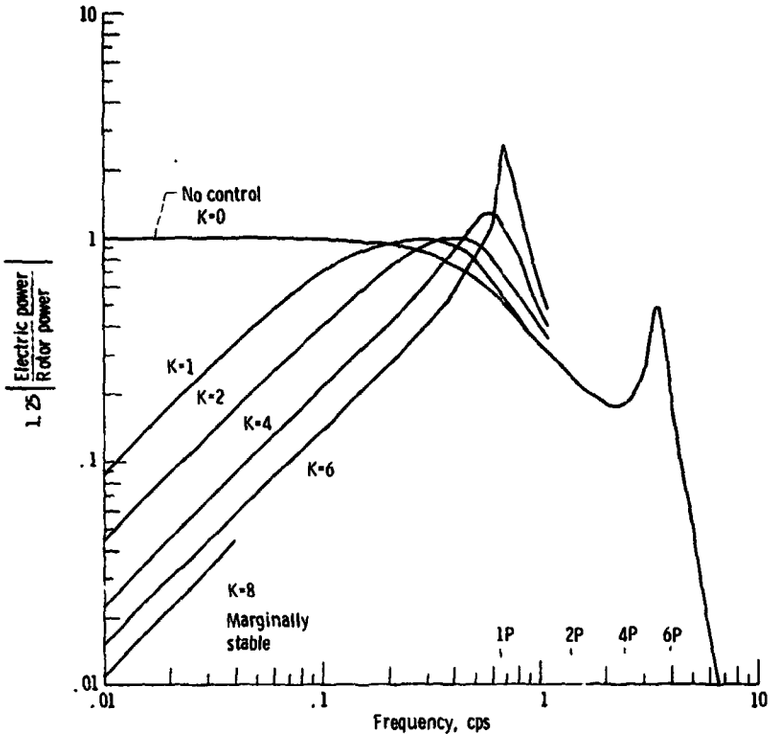

Figure 13. - Closed-loop frequency response magnitude comparisons for various pitch controller gains K with controller 0.027 K[(1/s) + 0.5]. Plant has slip coupling with slip rate of 2.3 percent at 100 kW.

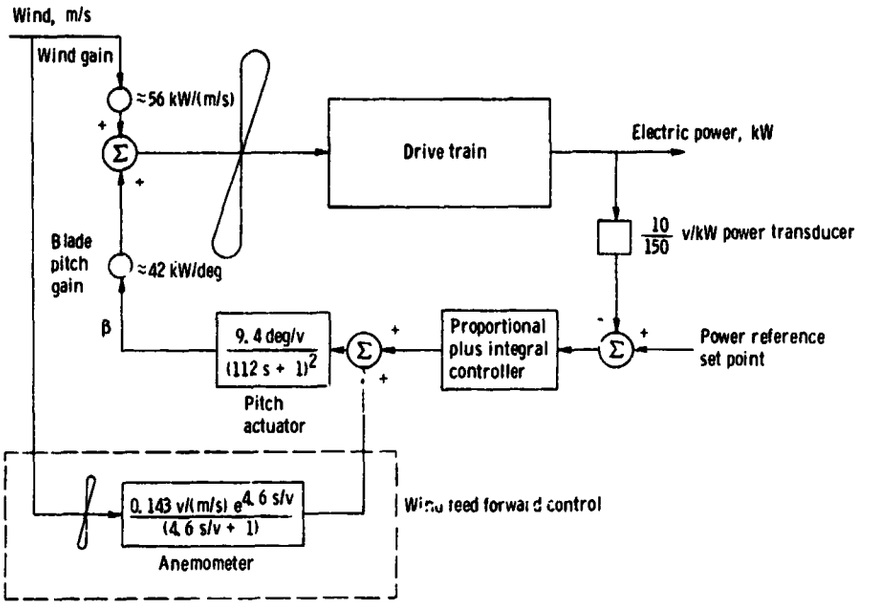

Figure 14. - Block diagram of closed loop power control and wind feed forward control.

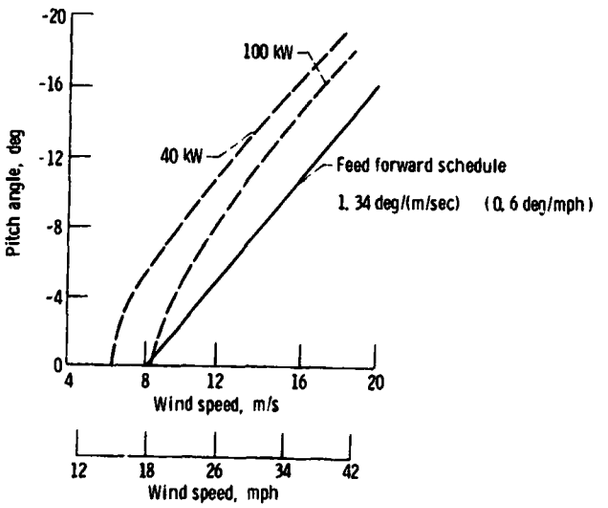

Figure 15. - Derivation of wind feed forward gain as slope of straight line approximation to curves of constant power in pitch angle versus wind speed.

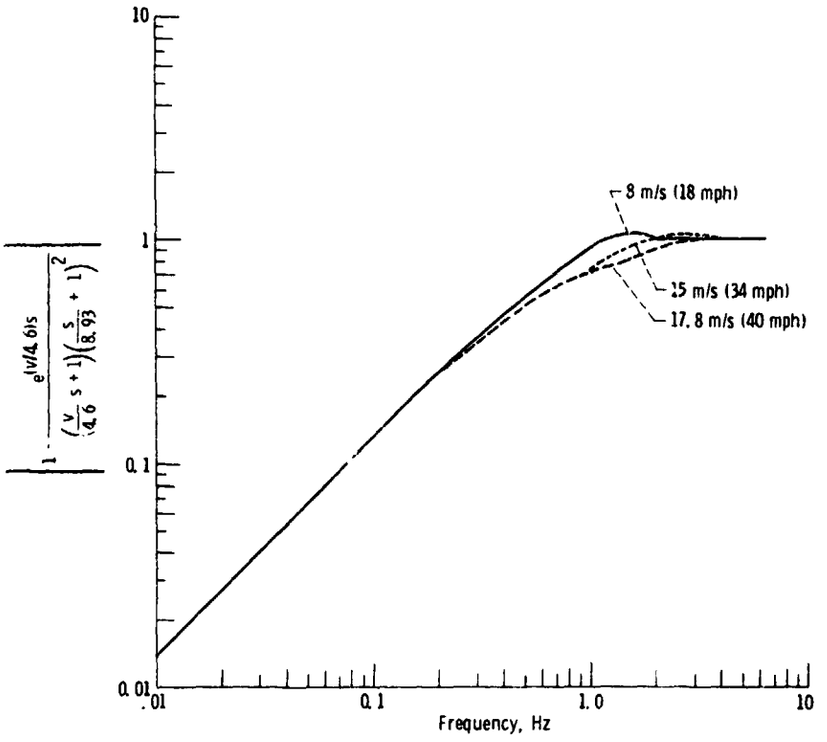

Figure 16. - Frequency response magnitude plot of theoretical attenuation of disturbances due to wind speed changes with wind feed forward control for three wind speeds.

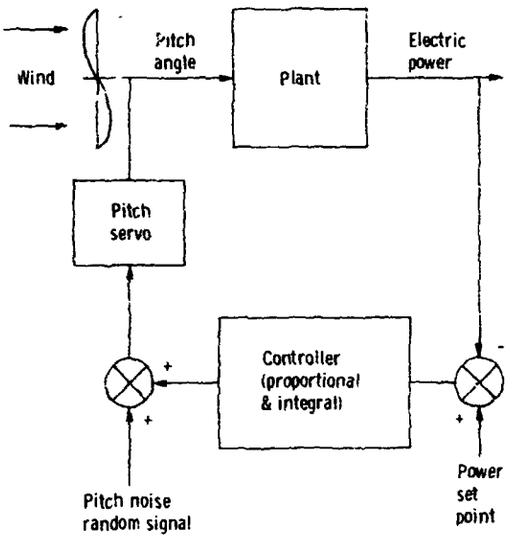

Figure 17. - Block diagram of pitch disturbance test for experimental frequency response.

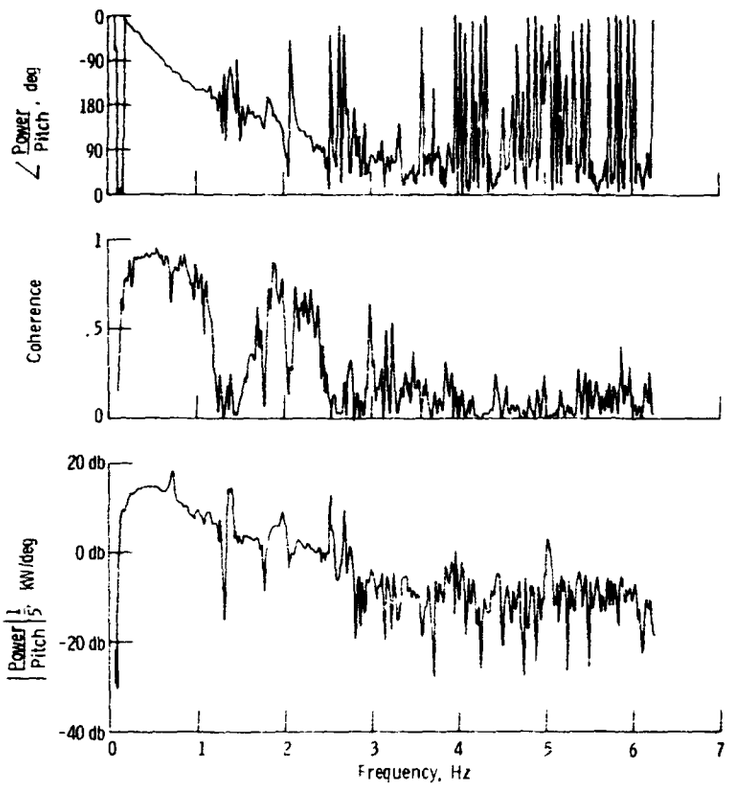

Figure 18. - Experimental phase, coherence, and magnitude frequency response plot of electric power-to-blade pitch angle, 1.05 percent slip at -70 kW. 0 db = 5 kW/deg.

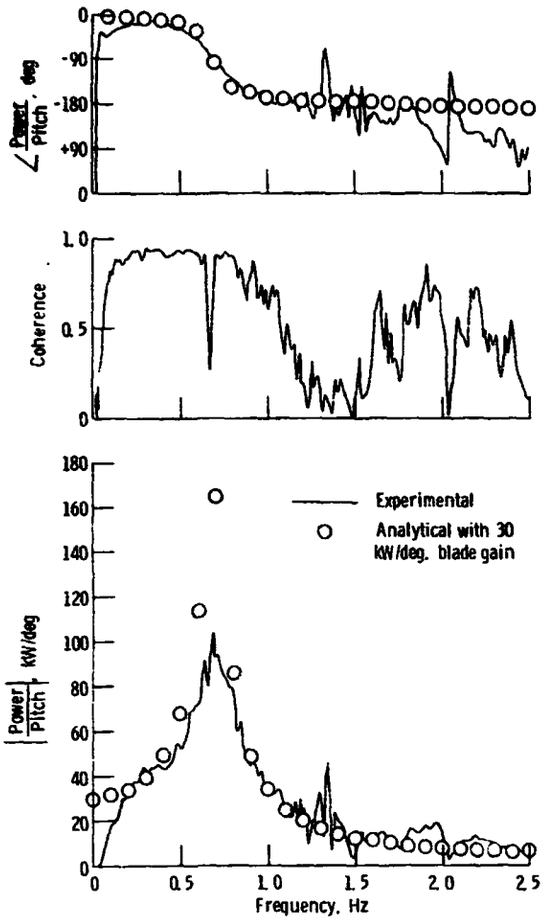

Figure 19. - Transfer function of electric power to blade pitch angle for steel high speed shaft. +70 kW.

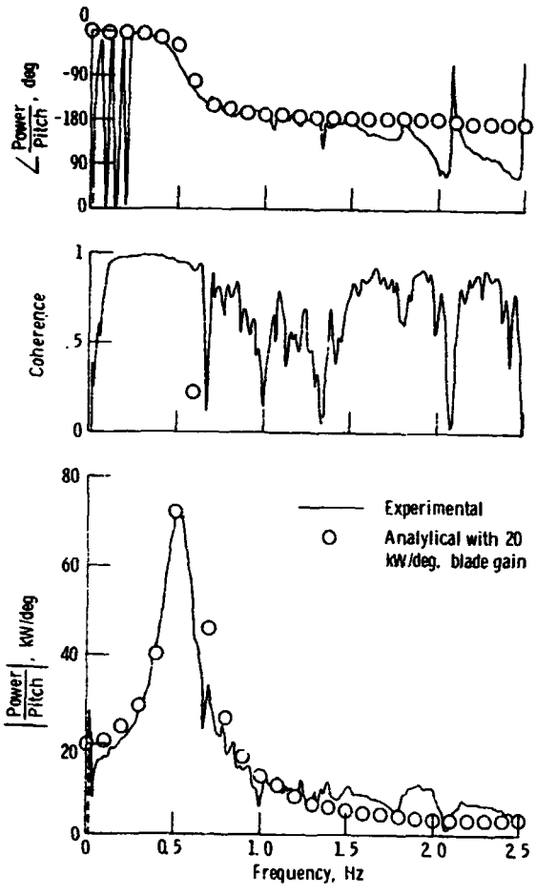

Figure 20. - Transfer function of electric power to blade pitch angle for elastomeric high speed shaft. -50 kW.

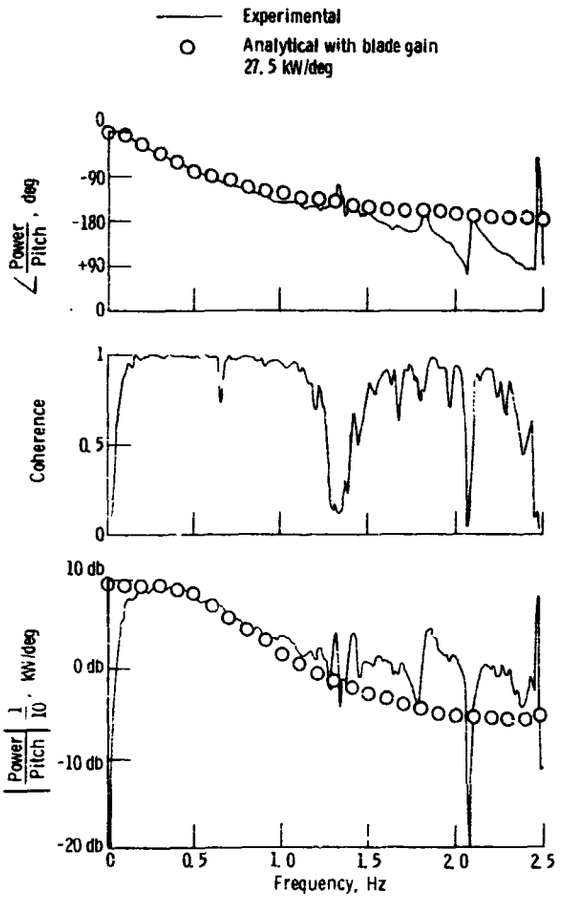

Figure 21. - Frequency response of electric power to blade pitch angle. 1.05 percent slip at -70 kW. 0 db = 10 kW/deg.

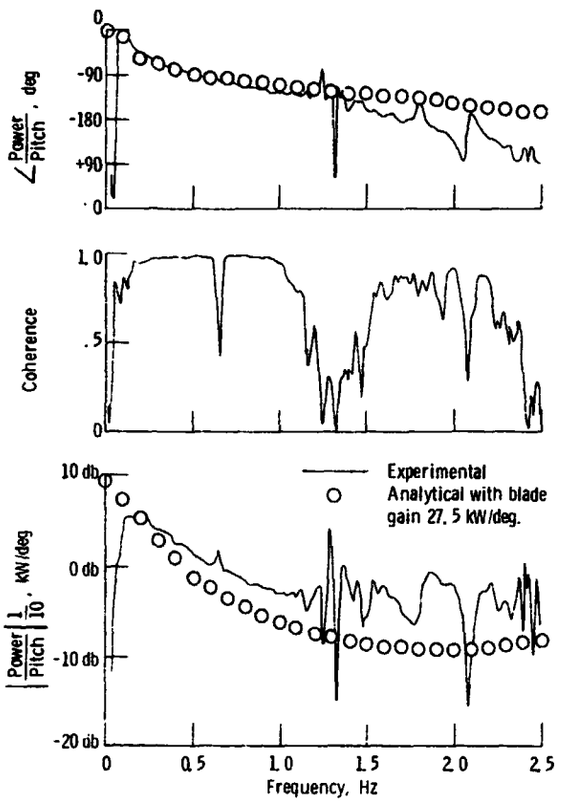

Figure 22. - Frequency response of electric power to blade pitch angle. 3.0 percent slip at -70 kW. 0 db = 10 kW.

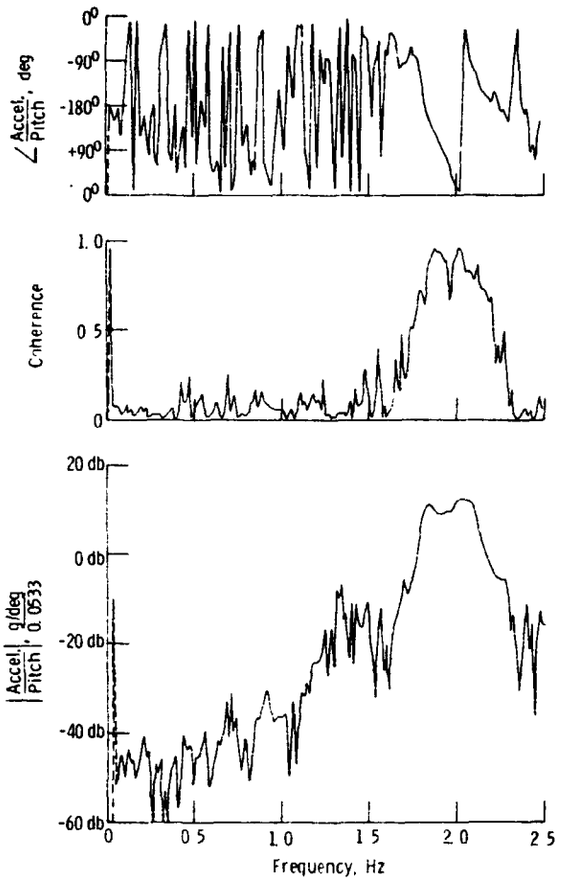

Figure 23. - Transfer function of horizontal acceleration of main bearing to pitch change 1.05 percent slip at -70 kW 0 db = 0533 g/deg

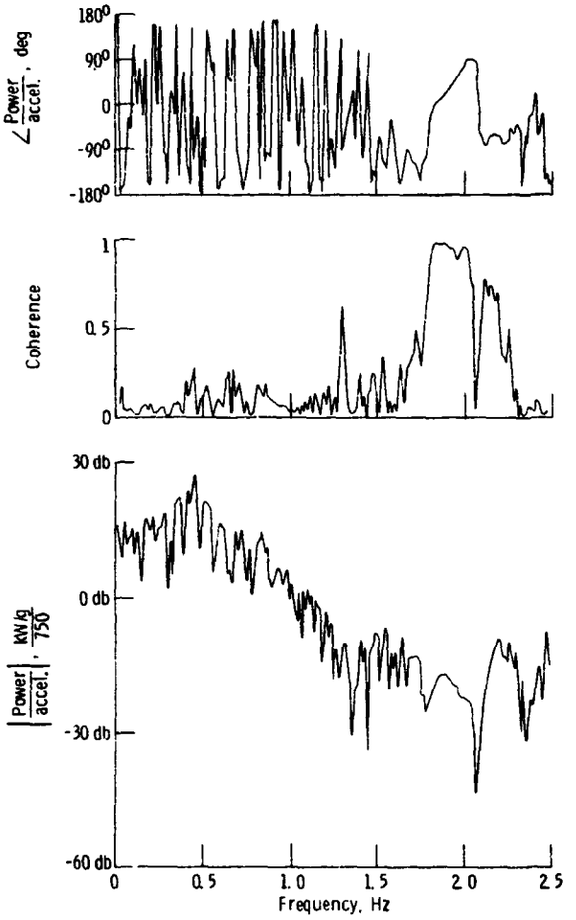

Figure 24. - Transfer function of electric power to horizontal acceleration of main bearing. 1.05 percent slip at -70 kW. 0 db = 750 kW/deg.

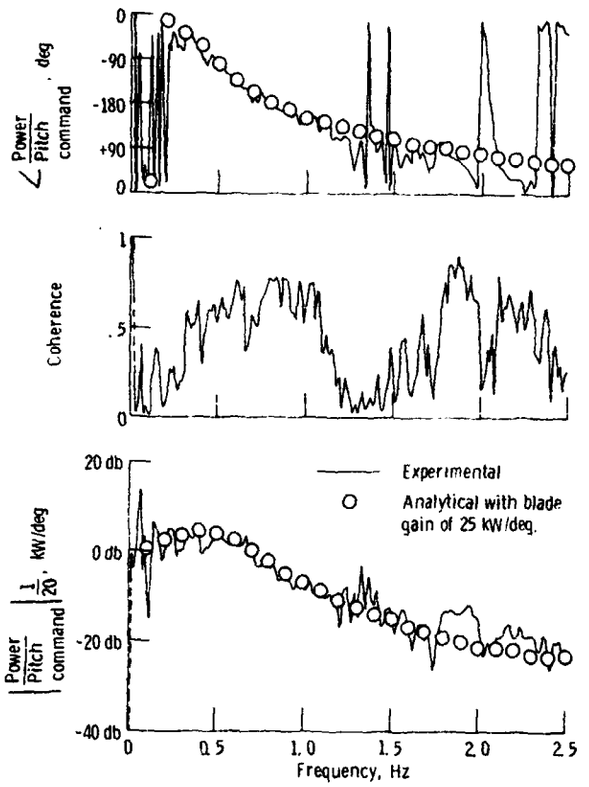

Figure 25. - Transfer function of electric power to blade pitch angle command with nominal control gains of proportional = 0.025 v/v and integral = 0.034 v/v/s. 1.2 percent slip at 50 kW. 0 db = 20 kW/deg.

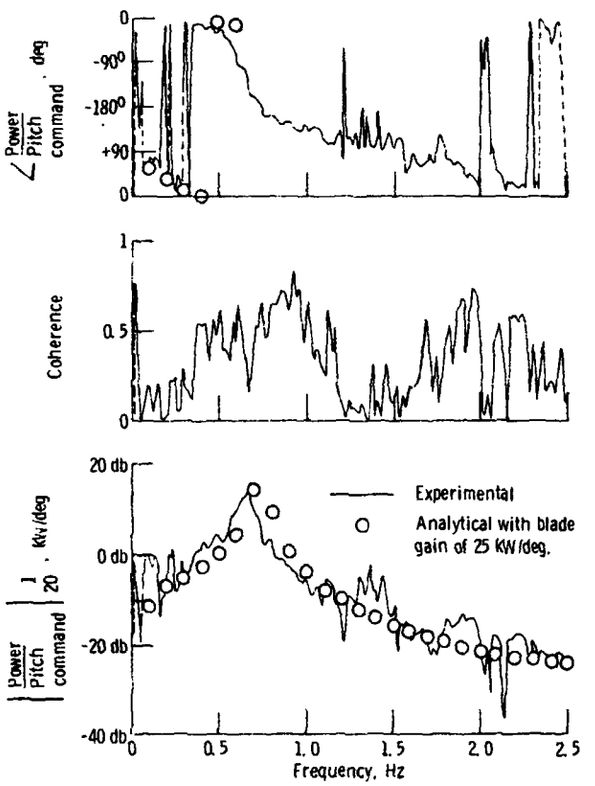

Figure 26. - Transfer function of electric power to blade pitch angle command with high control gains of proportional = 0.137 v/v and integral = 0.186 v/v/s. 0.75 percent slip at +50 kW. 0 db = 20 kW/deg.

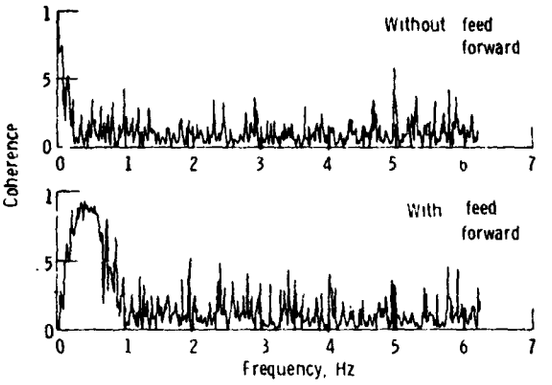

Figure 27 - Coherence between generator power and wind speed without and with feed forward control Fluid coupling slip of 2.3 percent at 100 kW. Proportional control gain of 0.027 v/v and integral control gain of 0.027 sec.

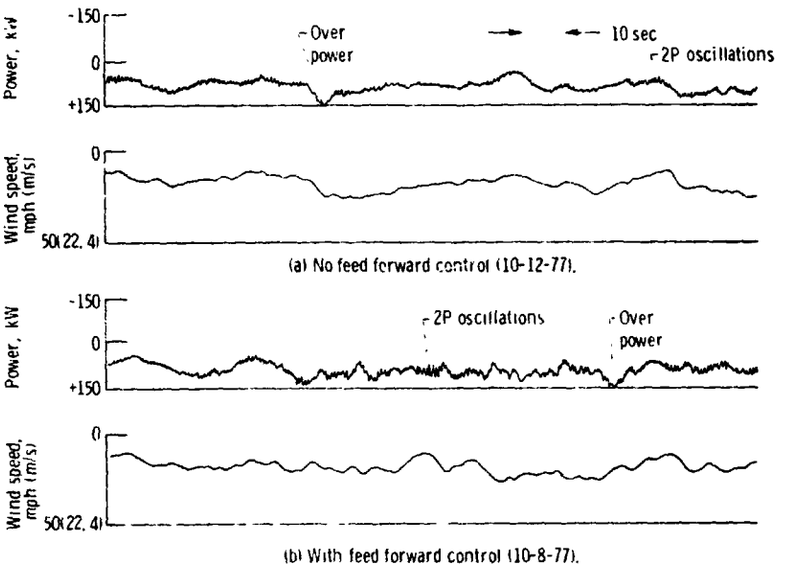

Figure 28. - Time history traces of power and measured wind speed with and without feed forward control. 2.3 percent slip at 100-kW. Proportional control gains of 0.027 v/v and integral control gain of 0.034 sec. Over power and 2P oscillations noted.

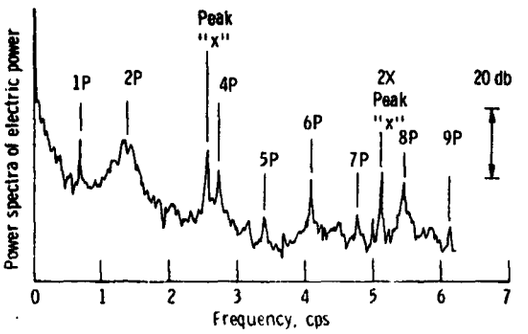

Figure 29. - 12-12-77 Spectra of generator electric power. 2.3 percent at 100-kW. Proportional control gains of 0.027 v/v and integral control gain of 0.034 sec. No wind feed forward control.

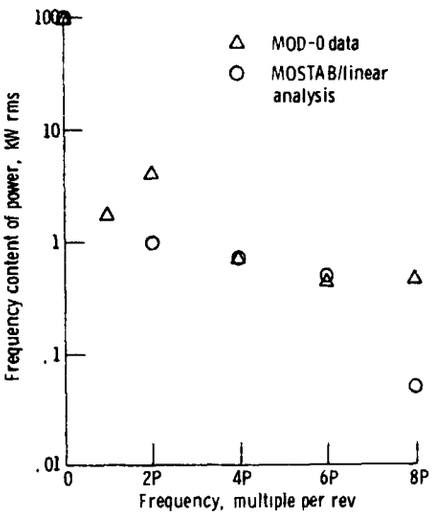

Figure 30. - Comparison of analytically predicted and measured frequency content of peaks in generator power.

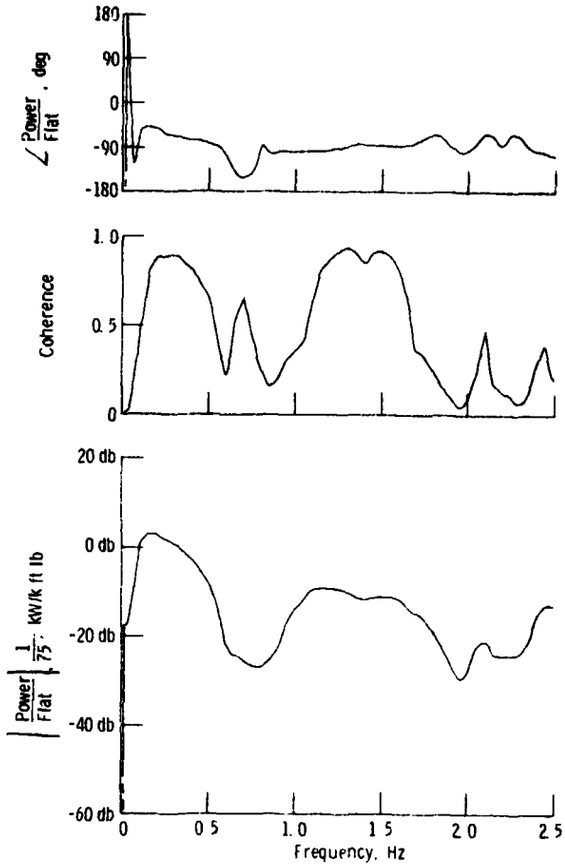

Figure 31 - Transfer function of electric power to blade flatwise bending moment with free yaw and 300 psi brake pressure. 1.5 percent slip at 100 kW. No induced pitch noise. 0 db = 75 kW/k ft lbs.

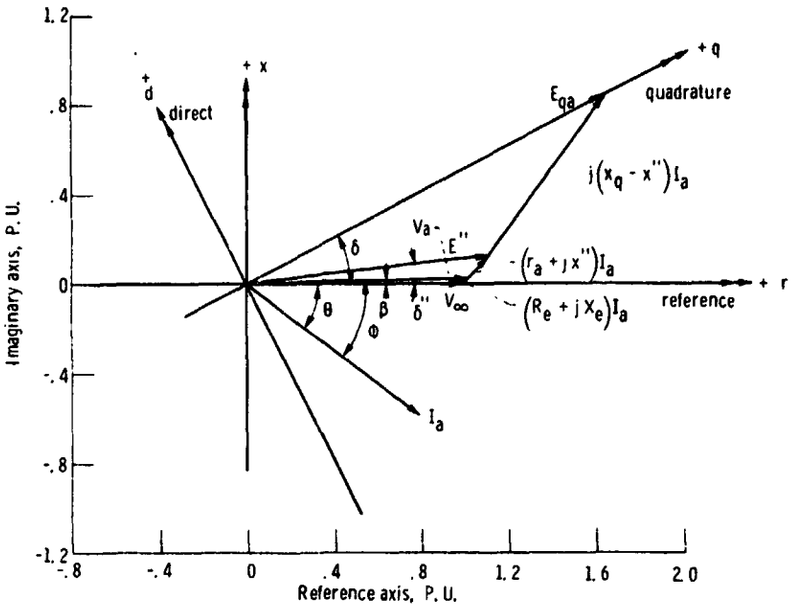

Figure 32. - Phase plot of generator initial conditions for power = 0.8 P.U., power factor = 0.8, and V_∞ bus voltage = 1.0 P.U. Imaginary number j shown as used in FORTRAN computer program with complex arithmetic.

```
C** MOD-0 INITIAL CONDITIONS
      SUBROUTINE CNSTS(Z,POWER)
      IMPLICIT REAL(I-L)
      COMPLEX IA,VA,EPP,EQA
      DIMENSION Z(1)
      COMMON/GEN/K1,K2,KD,XXD,XQXPP,XPDXL,Y,R,X,EFD,TH,K3,DELTA,VINF
      DATA XPPD,XPD,XD,XL/.128,.165,2.210,.05/,XQ,XPPQ/1.064,.193/
      DATA PF,RA/.8,.018/,RE,XE,VBUS/.0046612,.010307,1./
C**  GENERATOR CONSTANTS
 100  XPP=(XPPD+XPPQ)/2.
      XPDXL=XPD-XL
      K1=(XPP-XL)/XPDXL
      K2=1.-K1
      KD=(XD-XPD)*(XPD-XPP)/(XPDXL*XPDXL)
      XXD=(XD-XPD)*(XPP-XL)/XPDXL
      XQXPP=XQ-XPP
      R=RA+RE
      X=XPP+XE
      Y=1./(R*R+X*X)
      VINF=VBUS
C**  FIND IX AS PER PG 161 OF ANDERSON
      TTHEE=TAN(ARCOS(PF))
 200  IR=(POWER-RE*((POWER/(VINF*PF))**2))/VINF
      SQR=SQRT(VINF**2-4.*(-XE+RE*TTHEE)*(-IR*IR*XE+(VINF+RE*IR)*TTHEE*IR))
      IX1=(-VINF+SQR)/(2.*(-XE+RE*TTHEE))
      IX2=(-VINF-SQR)/(2.*(-XE+RE*TTHEE))
      IX=AMIN1(IX1,IX2)
C**  TERMINAL CONDITIONS
      IA=CMPLX(IR,IX)
      VA=VINF+IA*CMPLX(RE,XE)
      EQA=VA+IA*CMPLX(RA,XQ)
      EPP=VA+IA*CMPLX(RA,XPP)
      DELTA=ATAN2(AIMAG(EQA),REAL(EQA))
      DLT  =ATAN2(AIMAG(EPP),REAL(EPP))
      EPPD=-CABS(EPP)*SIN(DELTA-DLT)
      EPPQ=+CABS(EPP)*COS(DELTA-DLT)
      THETA=ATAN2(IX,IR)
      ID=-CABS(IA)*SIN(DELTA-THETA)
      IQ=+CABS(IA)*COS(DELTA-THETA)
C**  GENERATOR STATES
      EPQ=EPPQ-(XPD-XPP)*ID
      LD=EPQ+(XPD-XL)*ID
      EFD=EPQ*(1.+KD)-XXD*ID-KD*LD
      TH=EPPQ*IQ+EPPD*ID
      Z(13)=EPPD
      Z(14)=LD
      Z(15)=EPQ
      Z(16)=TH
C**  LOW SPEED SHAFT STIFFNESS
      K3=0.0494368*SQRT(ABS(TH*125.))
 300  RETURN
      END
```

ORIGINAL PAGE IS
OF POOR QUALITY

Figure 33. - Subroutine CNSTS Fortran listing.

```
C**  MOD-0 STATE EQUATIONS
      SUBROUTINE HPRC(Z,F)
      IMPLICIT REAL(I-K)
      DIMENSION Z(1),F(1)
      COMMON/GEN/K1,K2,KD,XXD,XQXPP,XPDXL,Y,R,X,EFD,P1,K3,DELTA,VINF
      DATA K11,K5/.66E6,1.8E5/,R1,CONVRT,D,OMEGAS/45.,5869.,17.9,30./
      DATA J1,J3,J4,J5,J6/.2826E6,.57?2E6.25300.,15.,24.?/
      DATA CD1,CD3,CD4,CD5,CD6/.27E5,1.01E3,1.,.62,1.6/,GAIN/7?33096./
      DATA B1,B3,B4,B5/3.E5,2.E4,1100.,150./,KZ10/62.83/
      DATA TPP0,TPPD0,TPD0/.002,.011,1.942/
C  STIFF HST:  J4=10214,K4=6.66E5,D4=186,J5=7.57
 50   F1=K11*(Z(5)-Z(1))+B1*(Z(6)-Z(2))
      F2=K11*(Z(5)-Z(3))+B1*(Z(6)-Z(4))
      F3=K3*(Z(7)-Z(5))+B3*(Z(8)-Z(6))
      F4=K4*(Z(9)-Z(7)*R1)+B4*(Z(10)-Z(8)*R1)
      F5=K5*(Z(11)-Z(9))+B5*(Z(12)-Z(10))
      F(1)=Z(2)
      F(2)=(F1-CD1*Z(2))/J1+GAIN*Z(17)/J1
      F(3)=Z(4)
      F(4)=(F2-CD1*Z(4))/J1
      F(5)=Z(6)
      F(6)=(-F1-F2+F3-CD3*Z(6))/J3
      F(7)=Z(8)
      F(8)=(-F3+F4*P1-CD4*R1*Z(8))/J4
      F(9)=Z(10)
      F(10)=(-F4+F5-CD5*Z(10))/J5
      F(11)=Z(12)
      DLTA=Z(11)*2.+DELTA
      VINFD=-VINF*SIN(DLTA)
      VINFQ=+VINF*COS(DLTA)
      EPPO=K1*Z(15)+K2*Z(14)
      ID=Y*(-R*(VINFD-Z(13))+X*(VINFQ-EPPO))
      IQ=-(*(X*(VINFD-Z(13))+R*(VINFQ-EPPO))
      TE=EPPO*IQ+Z(13)*ID
      F(12)=(-F5+(TM-TE)*CONVRT-CD6*Z(12))/J6
      F(13)=(-Z(13)-XQXPP*IQ)/TPPO
      F(14)=(-Z(14)+Z(15)+XPDXL*ID)/TPDO
      F(15)=(-Z(15)*(1.+KD)+XXD*ID+KD*Z(14)+EFD)/TPDO
      F(16)=KZ10*(TE-Z(16))
      F(17)=Z(18)
      F(18)=-D*Z(18)-OMEGAS*(Z(17)-(Z(19)*R1+(TM-Z(16))*BP))
      F(19)=TM-Z(16)
100   RETURN
      END
```

ORIGINAL PAGE IS
OF POOR QUALITY

Figure 34. - Subroutine HPRC Fortran listing.

1 Report No	2 Government Accession No	3 Recipient's Catalog No
NASA TM-78997		

4 Title and Subtitle	5 Report Date
POWER-TRAIN ANALYSIS FOR THE DOE/NASA 100-kW WIND TURBINE GENERATOR	October 1978
	6 Performing Organization Code

7 Author(s)	8 Performing Organization Report No
Robert C. Seidel, Harold Gold, and Leon M. Wenzel	E-9413
	10 Work Unit No

9 Performing Organization Name and Address	11 Contract or Grant No
National Aeronautics and Space Administration Lewis Research Center Cleveland, Ohio 44135	

12 Sponsoring Agency Name and Address	13 Type of Report and Period Covered
U.S. Department of Energy Division of Distributed Solar Energy Washington, D.C. 20545	Technical Memorandum
	14 Sponsoring Agency ~~Code~~ Report No. DOE/NASA/1028-78/19

15 Supplementary Notes

Final report. Prepared under Interagency Agreement E(49-26)-1028.

16 Abstract

Progress in explaining variations of power experienced in the on-line operation of a 100-kW experimental wind turbine-generator is reported. Data are presented that show the oscillations tend to be characteristic of a wind-driven synchronous generator because of low torsional damping in the power train, resonances of its large structure, and excitation by unsteady and nonuniform wind flow. The report includes dynamic analysis of the drive-train torsion, the generator, passive driveline damping, and active pitch control as well as correlation with experimental recordings. The analysis assumes one machine on an infinite bus with constant generator-field excitation.

17 Key Words (Suggested by Author(s))	18 Distribution Statement
Wind turbine Power train Dynamics	Unclassified - unlimited STAR Category 44 DOE Category UC-60

19 Security Classif (of this report)	20 Security Classif (of this page)	21 No of Pages	22 Price*
Unclassified	Unclassified		

* For sale by the National Technical Information Service, Springfield, Virginia 22161